Glutamine Addiction in Kidney Cancer Suppresses Oxidative Stress and Can Be Exploited for Real-Time Imaging

Omran Abu Aboud[1], Samy L. Habib[2], Josephine Trott[1], Benjamin Stewart[3], Sitai Liang[2], Abhijit J. Chaudhari[4,5], Julie Sutcliffe[5,6,7], and Robert H. Weiss[1,8,9]

Abstract

Many cancers appear to activate intrinsic antioxidant systems as a means to counteract oxidative stress. Some cancers, such as clear cell renal cell carcinoma (ccRCC), require exogenous glutamine for growth and exhibit reprogrammed glutamine metabolism, at least in part due to the glutathione pathway, an efficient cellular buffering system that counteracts reactive oxygen species and other oxidants. We show here that ccRCC xenograft tumors under the renal capsule exhibit enhanced oxidative stress compared with adjacent normal tissue and the contralateral kidney. Upon glutaminase inhibition with CB-839 or BPTES, the RCC cell lines SN12PM-6-1 (SN12) and 786-O exhibited decreased survival and pronounced apoptosis associated with a decreased GSH/GSSG ratio, augmented nuclear factor erythroid-related factor 2, and increased 8-oxo-7,8-dihydro-2'-deoxyguanosine, a marker of DNA damage. SN12 tumor xenografts showed decreased growth when treated with CB-839. Furthermore, PET imaging confirmed that ccRCC tumors exhibited increased tumoral uptake of ^{18}F-(2S,4R)4-fluoroglutamine compared with the kidney in the orthotopic mouse model. This technique can be utilized to follow changes in ccRCC metabolism in vivo. Further development of these paradigms will lead to new treatment options with glutaminase inhibitors and the utility of PET to identify and manage patients with ccRCC who are likely to respond to glutaminase inhibitors in the clinic. Cancer Res; 77(23); 6746–58. ©2017 AACR.

Introduction

Oxidative stress is characterized as an imbalance between the generation of cellular oxidants and the process of scavenging their byproducts. If this redox balance is perturbed, then damage of essential components of the cell, including proteins, lipids, and DNA, will occur, thereby disturbing organismal homeostasis and leading to a variety of adverse outcomes including oncogenesis and progression of cancer (1–4). Reactive oxygen species (ROS), whose appearance can be considered a signature of oxidative stress, are generated primarily in the mitochondrial electron transport chain during the course of cellular metabolism and play a vital role in normal cell signaling pathways such as proliferation and apoptosis (5, 6). However, during periods or locations of environmental stress, such as a highly metabolically active malignancy, excessive ROS are produced, which can lead to structural damage within the cell and can actually hinder the progression of the malignancy (7); in such cases, cancer cells often compensate for the higher levels of intrinsic ROS by evolving adaptive mechanisms that increase the cellular antioxidants and corresponding pathways (8).

The role of ROS and antioxidants has been controversial in cancer research (9, 10). Although the oxidative stress induced by ROS can act in a protumorigenic fashion by inducing mutations, it can also be antitumorigenic by inducing (cancer) cell death and decreasing hypoxia-inducible factor (HIF) 1 levels (11). Despite the lay concept of antioxidants promoting overall health, many well-designed studies have failed to confirm this idea (12). In fact, there are several recent examples of cancers that are worsened, specifically by increasing metastasis, by the addition of antioxidants (7, 13, 14). Thus, the balance of pro- and antioxidative systems needs to be finely tuned for the "success" of the tumor, but this same system also has the potential to be subverted for therapeutic benefit.

In light of the recently recognized tenet that one of the hallmarks of cancer is metabolic reprogramming (15, 16), it is becoming clear that metabolism of many cellular nutrients, including the amino acids, follows reprogrammed pathways in cancer (17–20). Glutathione (GSH) is considered the predominant endogenous cellular antioxidant, playing a critical role in the cellular defensive response to oxidative stress by neutralizing free radicals and ROS (21). In clear cell renal cell carcinoma (ccRCC) in particular, the conditionally essential amino acid glutamine is subjected to reductive carboxylation leading to production of the

[1]Division of Nephrology, Department of Internal Medicine, University of California, Davis, Davis, California. [2]South Texas Veterans Health Care System and Cellular and Structural Biology Department, University of Texas Health Science Center, San Antonio, Texas. [3]Lawrence Livermore National Laboratory, Livermore, California. [4]Department of Radiology, University of California, Davis, Sacramento, California. [5]Center for Molecular and Genomic Imaging, University of California, Davis, Davis, California. [6]Division of Hematology and Oncology, Department of Internal Medicine, University of California, Davis, Sacramento, California. [7]Department of Biomedical Engineering, University of California Davis, Davis, California. [8]Comprehensive Cancer Center, University of California Davis, Sacramento, California. [9]Medical Service, VA Northern California Health Care System, Sacramento, California.

Note: Supplementary data for this article are available at Cancer Research Online (http://cancerres.aacrjournals.org/).

Corresponding Author: Robert H. Weiss, University of California, Davis, GBSF, Rm 6312, Davis, CA 95616. Phone: 916-734-3766; Fax: 530-752-3791; E-mail: rhweiss@ucdavis.edu

doi: 10.1158/0008-5472.CAN-17-0930

AACR

oncometabolite 2HG (22) as well as being a precursor for the major antioxidant system comprised of GSH and GSSG (19, 23). Indeed, a recent study showed that metabolites that eventually contribute to GSH biosynthesis were able to significantly separate ccRCC tumors from normal tissues (24), emphasizing the importance of this metabolic pathway to ccRCC.

There exist two glutaminases, GLS (kidney-type KGA and GAC isoforms) and GLS2 [liver isoform (LGA) and glutaminase B (GAB)], yet GLS is the isoform upregulated in cancer as well as the main glutaminase within the kidney (25, 26). Because GSH synthesis requires glutamate in addition to glycine and cysteine, we tested the hypothesis that blocking glutamate production from glutamine by GLS inhibition will downregulate this important antioxidant pathway, resulting in higher ROS levels, which will be selectively toxic to cancer cells due to their increased local ROS levels. As GLS regulates the first step of glutamine conversion to glutamate, in this study we utilized CB-839 as a glutaminase inhibitor.

CB-839 is a potent, selective, and orally bioavailable inhibitor of both splice variants of the glutaminase encoded by the GLS gene (KGA and GAC; refs. 27, 28). Recently, CB-839, as well as the selective KGA and GAC inhibitor BPTES, has been tested in glutamine-avid malignancies such as breast (29) and kidney cancer (30), and has showed success in inhibiting tumor growth. However, in prior studies, the role of glutamine reprogramming to the GSH/GSSG pathway had not been linked to either the promotion of oxidative stress or the inhibition of tumor growth.

Although PET using ^{18}F-fluorodeoxyglucose (^{18}F-FDG) has revolutionized imaging for many malignancies such as melanoma and lung cancer, it has been somewhat challenging for RCC due to excretion of the radiotracer in the urinary system (31, 32). However, based on the finding that many ccRCCs are quite glutamine avid (19, 33, 34) and that the PET radiotracer ^{18}F-(2S,4R)4-fluoroglutamine (^{18}F-FGln) is taken up by glioma and mammary tumor cells both in vitro and in vivo (35–37), whether uptake of the radiotracer will be applicable to kidney cancer cells is a rationale for the current study.

Due to the increasing evidence that ccRCCs are glutamine addicted (19, 33, 34) and that this amino acid is reprogrammed to feed an intrinsic antioxidant system, we now show that (i) the mechanism of the salutary effect of GLS inhibition in ccRCC relates to its effects on antioxidation and enhancement of oxidative stress, and (ii) glutamine reprogramming in ccRCC can be evaluated using ^{18}F-FGln-PET to dynamically study the tumor's biology and response to glutaminase inhibition therapy. Such molecular imaging has the potential to improve clinical practice by (i) earlier diagnosing and staging RCCs, and (ii) stratifying which patients are likely to respond to glutaminase inhibition by dynamically monitoring glutamine uptake in patient tumors before and after treatment with a GLS inhibitor.

Materials and Methods

Materials
PARP antibody was purchased from Cell Signaling Technology, Inc., goat anti-mouse and goat anti-rabbit HRP-conjugated IgG from Bio-Rad, anti-nuclear factor erythroid-related factor 2 (NRF2) antibody from Abcam, and ECL Plus solution from Thermo Fisher Scientific. CB-839 was supplied by Calithera Bioscience and was dissolved either in DMSO for in vitro experiments (10 mmol/L stock, stored at –20°C) or in vehicle for in vivo experiments. The in vivo vehicle consisted of 25% (w/v) hydroxypropyl-β-cyclodextrin in 10 mmol/L citrate (pH 2). The GLS inhibitor BPTES (bis-2-(5-phenylacetamido-1,2,4-thiadiazol-2-yl)ethyl sulfide) and all other reagents were purchased from Sigma-Aldrich.

Cell lines and media
786-O cells were purchased from the ATCC in January 2014 and authenticated originally by the source using short tandem repeat. The RCC cell line SN12PM-6-1 (abbreviated as SN12 throughout the article) was obtained from Dr. Robert Kerbel (Sunnybrook Research Institute, Toronto, ON, Canada); these cells have been previously selected for their ability to retain luciferase expression and to form primary orthotopic tumors (38). These cells were authenticated by Dr. Kerbel's laboratory as described (38). All cells were expanded and then frozen at low passage (passage 5) within 2 weeks after receipt of the original stocks. All cells used for in vitro experiments were between passages 7 and 15. All cells were routinely monitored in our laboratory for cellular morphology and microbial presence by microscopic observation, and they were Mycoplasma tested after each thaw or every 6 weeks when growing in culture. The kit used for Mycoplasma test was the MycoAlert Mycoplasma Detection Kit from Lonza. SN12 and 786-O cells were all maintained at 5% CO$_2$ and at 37°C in DMEM containing 5.5 mmol/L glucose and supplemented with 10% FBS, 100 units/mL streptomycin, and 100 mg/mL penicillin.

Metabolite analysis
786-O and SN12 cells were plated in 6-well tissue culture dishes at a density of 2.5 × 10^5 cells per well in triplicates for each treatment group for both cell lines. The second day cells were washed with PBS and incubated with 1 μmol/L CB-839 or DMSO for 24 hours before harvesting. Metabolite extraction was made in 200 μL of ice-cold 50% methanol/50% water, and then 200 μL ice-cold chloroform was added. After centrifugation, the upper aqueous phase was collected in a fresh tube and kept in –80°C until the time of analysis. Metabolites were separated on a Waters Acquity H Class high-performance liquid chromatography (HPLC) system and measured with a Waters Xevo G2-XS QTOF instrument (Waters Corporation). For amino acid separations, the HPLC method reported by Guo and colleagues (39) was used with minor modifications as follows: acetonitrile with 0.15% formic acid was used as the organic mobile phase (B), and the gradient starting at 85% B; 6 minutes, 80% B; 10 minutes, 55% B; 12.5 minutes, 45% B, 12.6 minutes, 5% B; 14 minutes, 5% B; 14.1 minutes, 85% B; and 18 minutes, 85% B. The column was a Waters Acquity BEH Amide 1.7 μm, 2.1 × 150 mm column; the flow rate was 0.4 mL/minute; and the run time was 18 minutes. Metabolite standards were prepared in concentrations from 1 to 400 μmol/L in 50% acetonitrile/50% 10 mmol/L ammonium formate + 0.15% formic acid for quantitation. Detection was accomplished in positive electrospray, centroid MS^e data acquisition mode over m/z range of 50 to 1,000. Low-energy collision voltage was 6V, and high energy voltage ramped from 10 to 40V. Lock mass correction was applied using leucine enkephalin. Data acquisition was accomplished using MassLynx 4.1 software, and data analysis was performed with TargetLynx software (Waters Corporation).

GSH and GSSG quantitation

Levels of GSH and GSSG were assayed in cells and tissues using the GSH/GSSG-Glo Assay Kit (Promega) as previously described (19). The cells were plated on 96-well culture plates (1,500 cells/well), and the next day treated with DMSO, or 1 or 5 μmol/L of CB-839 ($n = 6$/treatment group) for 24 hours. The GSH and oxidized glutathione (GSSG) concentrations were measured in each well. Tumor and kidney tissue homogenates were utilized to measure absolute GSH and GSSG levels using the same kit. Briefly, frozen tissues were homogenized in 5% sulfosalicylic acid at either 100 or 47.3 mg/mL, proteins were precipitated by centrifugation, acid extracts were neutralized with 1 to 1.7 vol 0.5 mol/L HEPES (pH 8) and, if necessary, diluted with 0.25 mol/L HEPES (pH 7.5) to either 16.7 or 17.5 mg/mL, respectively. GSH and GSSG standard curves were prepared in the same concentration of 5% sulfosalicylic acid, 0.5 mol/L HEPES (pH 8), and 0.25 mol/L HEPES (pH 7.5), as was used for tissue extract preparation and neutralization.

Cell viability assay

Cell viability assays were performed as previously described (40). Briefly, SN12 and 786-O cells were plated in 96-well culture plates at a density of 3,000 cells/well, and after the indicated treatments (DMSO, CB-839, or BPTES) at the indicated concentrations for 72 hours, the cells were incubated in the MTT solution (40) for 3 hours. Then, the MTT solution was removed, and the blue crystalline precipitate in each well was dissolved in DMSO. Visible absorbance of each well at 540 nm was quantified using a microplate reader.

Cell-cycle analysis

Cell-cycle analysis was performed on the Muse Cell Analyzer (Millipore) following the manufacturer's instructions as previously described (41). Briefly, SN12 and 786-O cells were cultured in T25 cell culture flasks ($n = 3$ per condition) at an approximately 50% confluence, and after 24 hours, the cells were incubated with the indicated treatments (DMSO or CB-839) at the indicated concentrations for 72 hours. The cells were washed with PBS, fixed in 70% iced ethyl alcohol for 3 hours, and stained with propidium iodide (PI). After staining, the cells were processed for cell-cycle analysis using the Muse Cell Analyzer.

Apoptosis assay

Apoptosis in cells was measured using the Annexin V and Dead Cell Assay Kit on the Muse Cell Analyzer (Millipore) following the manufacturer's instructions as previously described (41). Briefly, SN12 and 786-O cells were cultured in T25 cell culture flasks ($n = 3$ per condition) at an approximately 50% confluence. After the indicated treatments for 72 hours, the cells were incubated with Annexin V and Dead Cell reagent (7-AAD) for 30 minutes, and the events for dead, late apoptotic, early apoptotic, and live cells were counted using the Muse analyzer.

Immunostaining of NRF2 and 8-oxo-7,8-dihydro-2'-deoxyguanosine in tumor and kidney tissues

Mouse tumors, adjacent normal kidney tissues, and right normal kidney tissues were harvested from animals and fixed in 10% formalin for 24 hours. Paraffin-embedded sections (4 μm) were stained for NRF2 using heat-induced antigen retrieval in citrate buffer (pH 6.0) and anti-human NRF2 (1:200 overnight), followed by 1-hour incubation with Rabbit HRP-Polymer (Bio-Care Medical) and ImmPACT diaminobenzidine peroxidase substrate (Vector Laboratories). All sections were viewed and photographed using light microscopy. For 8-oxo-7,8-dihydro-2'-deoxyguanosine (8-oxodG) staining, a double-fluorescent labeling method of immunostaining was performed in kidney and tumor sections of mice as previously described (42). Briefly, sections were stained with an 8-oxodG antibody, FITC-labeled secondary antibody, and nuclei stained with PI. FITC was detected using a 450–490 nm filter and PI using a 535 nm filter. All sections were viewed and photographed using a Nikon Research microscope equipped for epifluorescence with excitation and band pass filters. To demonstrate staining specificity, control tissue sections were stained without primary antibody.

Immunostaining of NRF2 in cells

SN12 cells were plated on multichamber glass slides (Fisher Scientific), and the second day cells were washed with PBS and incubated with DMSO or CB-839 (1 μmol/L) for 24 hours. H_2O_2 (500 μmol/L) was added in the last 4 hours of the treatment to indicated groups (DMSO/H2O2, CB-839/H2O2)). After 24 hours, the media were removed, and the cells were fixed for 15 minutes in PBS containing 4% paraformaldehyde and 2% sucrose and then permeabilized in PBS containing 0.3% Triton X-100 for 2 minutes. The cells were incubated with NRF2 antibody (1:200), an FITC-labeled anti-rabbit antibody, and the nuclei were stained with DAPI. The cells were mounted onto slides and visualized using fluorescence microscopy (Zeiss LSM 510 laser-scanning confocal microscope image system), and for each treatment group, five microscopic fields were randomly chosen and counted for NRF2-positive staining.

8-oxodG quantitation in cells and tissues

DNA was isolated from cells or frozen normal and tumor kidney cancer samples as previously described (42). DNA purity and concentration were determined spectrophotometrically. Digestion of 8-oxodG was performed using nuclease P1 and alkaline phosphatase as previously described (42). Authentic standards of 8-oxodG were analyzed, and its quantitation in each sample was performed by linear regression analyses according to the manufacturer's instruction (#589320; Cayman Chemical).

Immunoblotting

The cell lysates were prepared with RIPA lysis buffer (Fisher Scientific) containing a protease inhibitor cocktail (Invitrogen). Immunoblotting was done as described previously (19). Densitometry was performed using ImageJ software.

Orthotopic RCC mouse model and *in vivo* experiments

All animal procedures were performed in compliance with the University of California Institutional Animal Care and Use Committee (IACUC). In all three animal experiments, an orthotopic model for SN12 cells was used in which cells were implanted under the left kidney (LK) capsule. Briefly, for orthotopic injection under the renal capsule, 2-month-old male Fox Chase SCID (CB17SCID) mice from Charles River Laboratories were used as described elsewhere (38). First, mice were anesthetized with isoflurane (2%–3%), and then a small incision was made along the left flank of the mouse. The abdominal cavity was opened, and the LK was exteriorized. An ultrafine needle attached to a 10 μL Hamilton syringe was used to slowly inject a half million viable

SN12 cells in a total of 10 µL volume in DMEM growth media under the LK capsule. After 1 week, tumor growth was confirmed and followed up by whole-body bioluminescence imaging (BLI) as described below. A 90% success rate for tumor growth was achieved in all three experiments.

Three animal experiments were performed in this study. The first experiment was designed to measure the baseline oxidative stress biomarkers where all animals (10 mice) received no treatment. In this experiment, mice were euthanized at day 28 after cell implantation, and samples were collected as indicated. The second experiment was designed to investigate the effect of the GLS inhibitor CB-839 (total 10 mice, $n = 5$ in CB-839 and vehicle-treated groups) on the oxidative stress biomarkers and to test whether PET using ^{18}F-FGln can be used to visualize RCC tumors. In the third experiment, designed to increase the power of the ^{18}F-FGln-PET studies, more mice (total 16 mice, $n = 8$ in CB-839 and vehicle-treated groups) were utilized to confirm the findings from the second experiment. For the last two animal experiments, when tumors reached a considerable size at 3 weeks after cell implantation (according to our and others' (38) experience with this model), mice were randomly assigned to one of the two treatment groups (vehicle or CB-839). CB-839 was formulated at 20 mg/mL (w/v) in vehicle (29). The animals in both latter experiments were orally dosed with vehicle or 200 mg/kg of CB-839 twice a day. For the second experiment ($n = 5$ per group), the treatment was for 3 weeks to allow for sufficient tissue for the indicated assays, and the animals were weighed every 4 days and euthanized at day 20 (4 hours after last dosing with vehicle or CB-839). For the third animal experiment, the treatment continued for 2 weeks to test the effect of CB-839 on tumor growth and evaluate 4-[^{18}F]fluoroglutamine uptake, and the animals were weighed every 3 days and euthanized at day 14 (4 hours after last dosing with vehicle or CB-839). All animals were monitored for signs of adverse reactions. Tumor samples and organs were collected for indicated analyses.

BLI

In all three *in vivo* experiments, whole-body BLI was performed on all animals every week during the experiment to monitor tumor progression as follows: luciferin (15 mg/mL in PBS; Gold Biotechnology, Inc.) was administered intraperitoneally at 150 mg/kg. The mice were anaesthetized with isoflurane (2%–3%) and imaged 10 minutes after injection in the IVIS Spectrum (PerkinElmer). The exposure time was 3 minutes, and 2 to 3 mice were imaged at a time. Data processing was performed using the vendor-provided Living Image software. The BLIs were quantitated using Living Image software as follows: regions of interest (ROI) for BLIs from all 16 mice were designated inside the primary (not metastatic) tumor sites on the LK using the free draw function and quantified as a mean of total flux (photons/second).

Radiochemistry

^{18}F-FGln was synthesized as previously described by Kung and colleagues (35, 36). 4-[^{18}F]fluoroglutamine (^{18}F-FGln) was evaluated by chiral HPLC to determine radiochemical purity and optical purity, and to verify identity, by coinjection with reference standards (35, 43).

^{18}F-FGln cell uptake

SN12 cells and 786-O cells were grown in T75 cell culture plates at an approximately 75% confluence, and 24 hours later, cells were incubated with 1 µmol/L CB-839 or DMSO for the last 4 hours before harvesting the cells for the uptake assay to maintain a high cell viability. The cells were then collected and washed with PBS, and the viability was tested using Muse Cell Analyzer (viability was 98%). The cells were resuspended in DMEM media (low glucose) supplemented with 2 mmol/L glutamine, and the assay was performed as follows: ^{18}F-FGln (7.4 KBq) was added to cell suspensions (3.0×10^6 cells) in DMEM (50 µL) and incubated at room temperature for 30 minutes in closed Eppendorf tubes [pretreated with BSA (5% w/v in PBS) to block nonspecific binding] with regular agitation. Following centrifugation at 130 x *g* for 3 minutes, the supernatant was removed, and the cell pellet was washed with DMEM (0.5 mL). The supernatants were combined, and the cells were resuspended in DMEM (0.6 mL). The cells (containing bound ^{18}F-FGln) and the DMEM supernatant solution (containing unbound ^{18}F-FGln) were separated and counted. The fraction of radioactivity inside the cells was determined with a γ-counter and the percent uptake calculated as radioactivity in the cellular fraction divided by total radioactivity in cells plus supernatant.

PET and CT imaging and analysis

Five mice in each treatment group (CB-839 or vehicle treated) were imaged before the start of the treatment (day 0) and 14 days after treatment. All imaging was performed under an IACUC-approved protocol. The animals were anesthetized with isoflurane (2.5%) and administered approximately 225 µCi ^{18}F-FGln via tail vein catheter injection, and then the animals were imaged. Imaging of animals at day 0 (base line) was performed with no prior treatment, but at day 14 of treatment, imaging was started at least 4 hours after orally dosing of vehicle or CB-839 (29). PET images were acquired for 30 minutes using a small-animal PET scanner (DPET; Siemens Preclinical Solutions), starting at 15 minutes after injection of ^{18}F-FGln. PET images were reconstructed using a conventional 3D MAP reconstruction with a single hyperbolic prior (SP-MAP) provided by the vendor. After the PET scan, the animal bed was moved to a CT scanner (Inveon CT; Siemens Preclinical Solutions) for anatomical image acquisition. Ellipsoid 19.06 mm³ ROIs were drawn using the AMIDE software on the PET/CT overlay images to calculate the mean standardized uptake value (SUV) for each right kidney (RK) and each tumor in the LK.

Statistical analysis

The day 14 mean SUVs from ^{18}F-FGln-PET images were analyzed by ANOVA using SAS version 9.3 and the Proc GLM program to test for differences between tissues (kidney vs. tumor) and differences between vehicle and CB-839 treatments. Tukey and Dunnett *post hoc* tests were used. All other data were statistically analyzed using two-sample equal variance Student *t* tests with a two-tailed distribution. A *P* value of < 0.05 was considered statistically significant.

Results

Subcapsular ccRCC xenograft tumors demonstrate higher levels of oxidative stress compared with adjacent normal and contralateral normal renal tissues in an orthotopic mouse model of ccRCC

The free radical scavenging function of GSH is evidenced by the appearance of GSSG, the oxidized form of GSH, such that a decreased GSH/GSSG ratio serves as a signature of oxidative

stress in a biological system (44, 45). We established a ccRCC orthotopic mouse model by implanting luciferase-expressing SN12-PM6-1 cells (SN12; ref. 38) under the LK capsule of SCID mice, leaving the contralateral RK untouched. Tumor growth rates in these mice were evaluated using weekly BLI (Fig. 1A), and for this first (treatment-naïve) in vivo experiment, the tumors were collected at sacrifice, 4 weeks after subcapsular cell implantation, to evaluate their redox status compared with tumor-adjacent and normal kidney tissues. The xenograft tumors showed increased levels of reduced and oxidized forms of glutathione (GSH and GSSG, respectively) compared with tissues from the normal RK and from the adjacent normal LK (Fig. 1B), likely as a result of their dealing with a higher level of oxidative stress due to their faster metabolism and activation of proliferative pathways. In addition, the GSH/GSSG ratios were significantly decreased in tumor tissues as compared with tissues from the normal RK but with less extent in the adjacent normal LK (Fig. 1C), indicating that the RCC microenvironment was associated with higher levels of oxidative stress compared with normal kidney tissues.

Because the direct measurement of ROS is challenging due to the short lifetime of this species and to its immediate reaction with redox state regulating components, we utilized indirect measurements of oxidative stress. We evaluated levels of NRF2, a transcription factor that controls enzymes that regulate the antioxidant response in cells (46), and we also used indirect measurements of oxidative damage to DNA by measuring levels of 8-oxodG (47).

Immunohistochemistry analysis revealed increased NRF2 expression in tumor as compared with normal contralateral kidney tissues (Fig. 1D; Supplementary Fig. S1). Similarly, immunohistochemistry for 8-oxodG showed greater numbers of subcapsular tumor cells expressing this marker of oxidative damage compared with cells in the contralateral normal kidney (Fig. 1E). 8-oxodG levels were quantified and found to be significantly increased in tumors ($P = 0.006$; Fig. 1F). Taken together, these results suggest that, at least in the ccRCC subcapsular xenografts used in this study, the tumors showed increased levels of oxidative stress, as well as an enhanced antioxidant buffer system, when compared with normal kidney tissue.

Glutaminase inhibition by CB-839 blocks glutamine utilization in RCC cells and tissue

After validating and confirming the high oxidative stress signature in tumors in the mouse model, we next asked whether the glutamine pathway is involved in the regulation of oxidative stress in both in vitro and in vivo models of RCC. Glutamate is produced from glutamine, the most abundant amino acid in plasma (18, 23), by the mitochondrial enzyme GLS (27). Because GSH requires glutamate (in addition to glycine and cysteine) for its synthesis, we next asked whether the selective GLS inhibitor CB-839 (29, 30) blocks this key antioxidant pathway and thereby reduces GSH in RCC cells; such a finding would be expected to adversely affect several critical metabolic pathways including the tricarboxylic acid cycle and redox balance (Fig. 2A). Incubating SN12 and 786-O cells with CB-839 significantly increased glutamine levels in both the cells and the media as compared with control cells, and intracellular glutamate was significantly decreased. These data are expected given that the conversion of glutamine to glutamate is blocked by GLS inhibition (Fig. 2B; Supplementary Fig. S2A) and are consistent with a recently

published breast cancer study using CB-839 (37). Furthermore, GSH, which has glutamate as a precursor, was decreased by CB-839 treatment, and GSSG was relatively increased (also reflected by a decreased GSH/GSSG ratio), demonstrating increased levels of oxidative stress within the cells in the presence of GLS inhibition (Fig. 2B). These results are consistent with our previous work in other RCC cell lines using glutamine-depleted media in which the GSH/GSSG ratio was reduced under these growth conditions (19). The tumors from mice treated with CB-839 also showed a decreased trend in GSH/GSSG ($P = 0.139$) compared with tumors from mice treated with vehicle (Fig. 2B, far right plot), indicative of increased oxidative stress as a result of GLS inhibition and consistent with the in vitro data. Taken together, these results demonstrate that CB-839 decreases glutamate production and results in enhanced oxidative stress within SN12 and 786-O RCC cells via attenuation of the GSH pathway. In light of these results, we next asked if GLS inhibition could be beneficial to treat RCC by testing its biological effects in RCC cells and tumors using both in vitro and in vivo models.

Glutaminase inhibition increases oxidative stress and attenuates viability in RCC cells

To elucidate a more detailed response to GLS inhibition in ccRCC cells, we incubated SN12 as well as 786-O cells with CB-839 or another GLS inhibitor, BPTES (48), at several doses for 72 hours and evaluated cell viability, cell-cycle arrest, and measures of DNA damage and apoptosis (Fig. 3). Both CB-839 and BPTES share a similar allosteric binding mechanism and selectivity profile upon GLS (29), and we show that both dose-dependently attenuated cell viability or proliferation as measured by an MTT assay (Fig. 3A). Incubation of RCC cells with CB-839 (from 10 nmol/L to 5,000 nmol/L) for 72 hours showed a cell viability IC_{50} of 740 nmol/L for SN12 cells and 970 nmol/L for 786-O cells (Supplementary Fig. S2B); thus, 1 μmol/L of CB-839 was used in the subsequent in vitro experiments. Because CB-839 showed a higher magnitude of cell viability reduction (see Fig. 3A), and because it is a clinical candidate for ccRCC (30), we used only CB-839 as a GLS inhibitor in all subsequent experiments.

CB-839 caused cell arrest in G_0–G_1 (Fig. 3B), and 72 hours of treatment significantly increased the percentage of apoptotic cells that were Annexin V and 7-AAD positive (Fig. 3B), which indicate increased late-stage apoptotic and dead cells. To further support the role of the GSH pathway in neutralizing ROS, we incubated SN12 cells with CB-839 for 20 hours and then induced oxidative stress by adding H_2O_2 for 4 hours. Under these conditions, CB-839 dose-dependently sensitized RCC cells to H_2O_2, as evidenced by an increased percentage of apoptotic and dead cells demonstrated both by flow cytometry using Annexin V and 7-AAD staining (Fig. 3C; Supplementary Fig. S3). These data were supported by the observed increase in PARP cleavage under the same conditions (Fig. 3D).

To further validate the effect of CB-839 on oxidative stress biomarkers in vitro, we evaluated oxidative DNA damage by measuring cellular levels of 8-oxodG. Incubation of SN12 and 786-O cells with 1 μmol/L CB-839 for 24 hours significantly increased 8-oxodG in these cells (Fig. 4A, left two plots), suggesting that the cells had a reduced capacity to repair ROS-induced damage while in a state of enhanced oxidative stress due to the presence of glutaminase inhibition. A significant increase of 8-oxodG was also detected in tumors from mice treated with
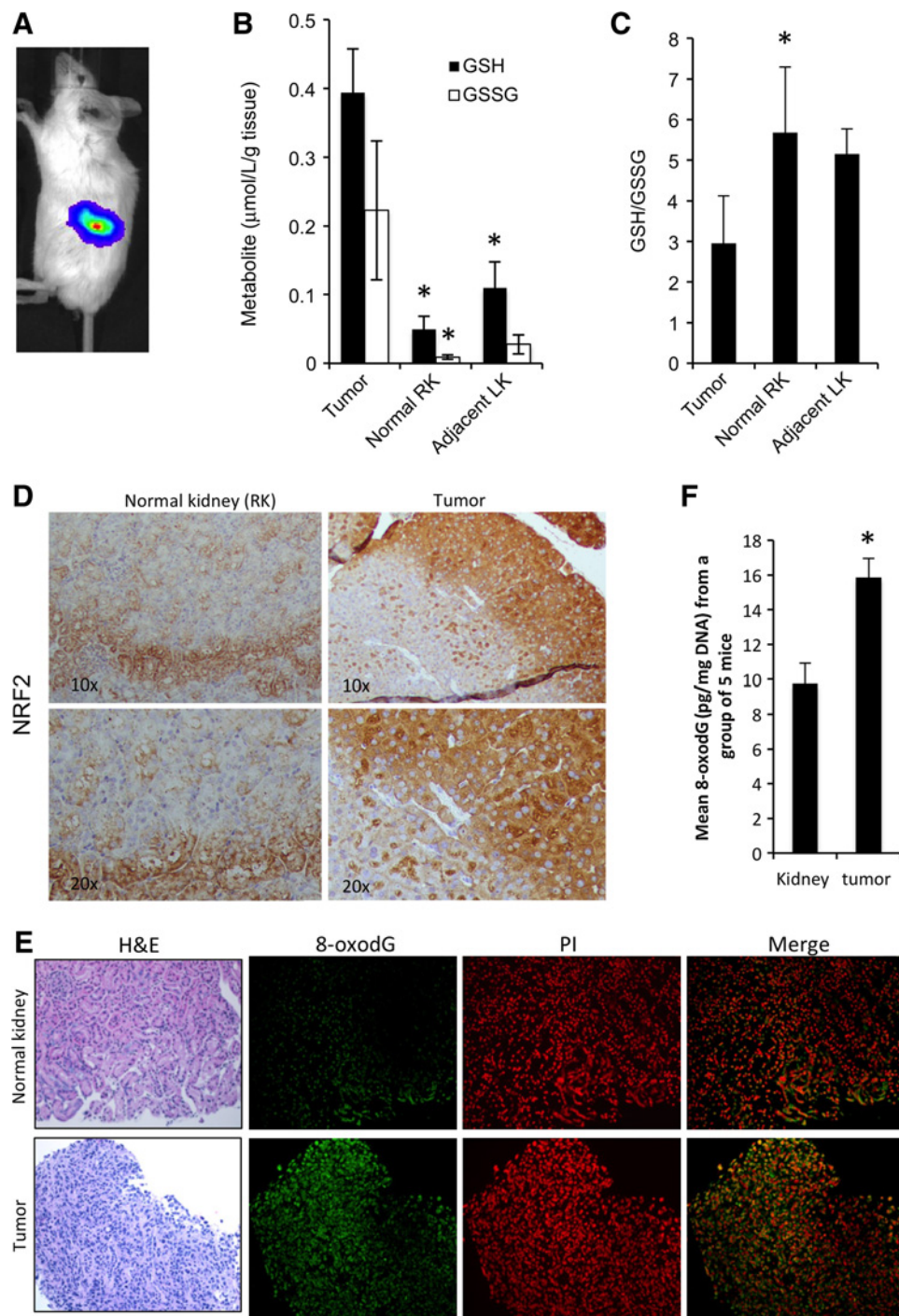
Figure 1.
RCC tumors show higher oxidative stress as compared with adjacent normal and contralateral renal tissues. **A,** SN12 cells were implanted under the renal capsule of the LK in SCID mice, and whole-body BLI was acquired in the three animal experiments as described in Materials and Methods. A representative imaged mouse is shown. **B,** The metabolites GSH and GSSG were measured in RCC tumors, tumor-adjacent normal tissue in LK, and untouched RK in untreated mice ($n = 3$). Data are mean $\pm$ SEM. *, $P < 0.05$ compared with tumor tissue. For GSH, $P = 0.008$ for tumor vs. RK and $P = 0.032$ for tumor vs. LK. For GSSG, $P = 0.006$ for tumor vs. RK and $P = 0.071$ for tumor vs. LK. Results shown are representative of at least three independent experiments. **C,** The ratio of GSH/GSSG from the same measurements in **B** was calculated in RCC tumors, adjacent renal tissue in LK, and tissue from RK ($n = 3$/group). Error bars, SEM. *, $P < 0.05$ compared with tumor tissue. For tumor vs. RK, $P = 0.023$ and for tumor vs. LK, $P = 0.069$. Results shown are representative of at least two independent experiments. **D,** Representative sections of normal RK and tumor tissues were subjected to immunoperoxidase staining for NRF2. **E,** Representative sections of normal and tumor kidney tissues were subjected to immunofluorescence staining for 8-oxodG and PI (nuclear stain). **F,** Quantitation of 8-oxodG levels was measured in the DNA of RCC tumors and normal kidney tissues from 5 mice, which were randomly selected from 10 untreated mice, and the average is shown. Data are mean $\pm$ SEM. *, $P < 0.05$ tumor compared with normal kidney ($P = 0.006$).

CB-839 (Fig. 4A, right plot), demonstrating that CB-839 is increasing oxidative stress at the DNA level.

We next examined NRF2 expression in our RCC cell model in the presence of the GLS inhibitor. In SN12 and 786-O cells, there were low basal levels of NRF2 protein in DMSO-treated cells, which was dose-dependently augmented after incubation of these cells with CB-839 (Fig. 4B). Subcellular localization of NRF2 in SN12 cells after incubation with CB-839 and H_2O_2 showed an increase in nuclear NRF2 in CB-839–treated cells, which was more pronounced upon H_2O_2 treatment (Fig. 4C and D). Thus, in the presence of CB-839, NRF2 orchestrates an enhanced response to the oxidative stress that is unleashed by means of a CB-839–mediated decrease in production of oxidative stress buffers.

CB-839 attenuates RCC tumor growth in the RCC orthotopic mouse model

To extend our findings to an *in vivo* model of ccRCC, we utilized CB-839 in the subcapsular orthotopic mouse model of ccRCC described earlier. In a third *in vivo* experiment, mice ($n = 8$/group) were dosed orally twice a day with vehicle or 200 mg/kg CB-839 for 2 weeks, and BLI was performed weekly (Fig. 5A; Supplementary Fig. S4A). The change in mean total flux for bioluminescence (photon/second) over the treatment period was calculated as a ratio for each animal (flux at day 14/flux at day 0; Fig. 5B). Treatment with CB-839 significantly inhibited growth of the tumors (Fig. 5B). As a general measure of lack of toxicity of this treatment, no mice treated with CB-839 showed a significant weight change (Supplementary Fig. S4B)
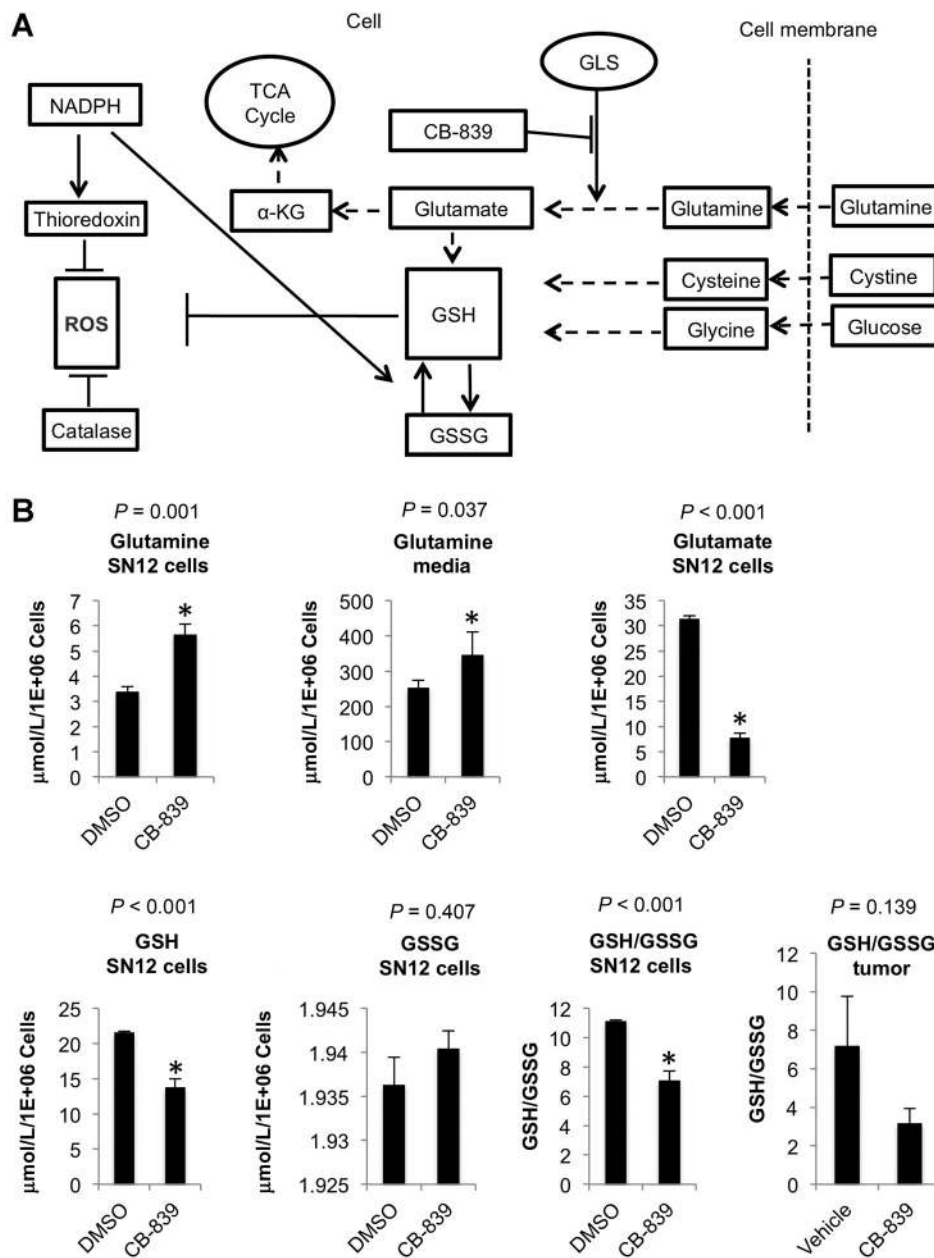

Figure 2.
Inhibition of glutaminase with CB-839 attenuates the GSH pathway in RCC. **A,** The antioxidant pathways that neutralize ROS. The glutamine pathway is reprogrammed in ccRCC to increase production of GSH and oxidized glutathione (GSSG). Glutamate, cysteine, and glycine are required to synthesize GSH. The conversion of glutamine to glutamate is regulated by GLS, which can be targeted and inhibited by CB-839 (or BPTES). Thioredoxin also reduces ROS levels and is generated by NADPH, which in turn regulates the conversion of GSH and GSSG. Catalase is another pathway, NADPH independent, which reduces ROS. TCA, tricarboxylic acid cycle. **B,** SN12 cells were incubated with 1 μmol/L CB-839 or DMSO for 24 hours ($n = 3$/group). The cells and conditioned media were obtained and analyzed by HPLC-MS/MS for the metabolites indicated as described in Materials and Methods. Data are mean ±SD. *, $P < 0.05$ compared with DMSO-treated cells. For tumor tissue (far right plot), tissues were collected from the second animal experiment (orally dosed with vehicle or CB-839; $n = 5$/group), and GSH and GSSG were measured using the GSH/GSSG Kit from Promega. Data are mean ± SEM.
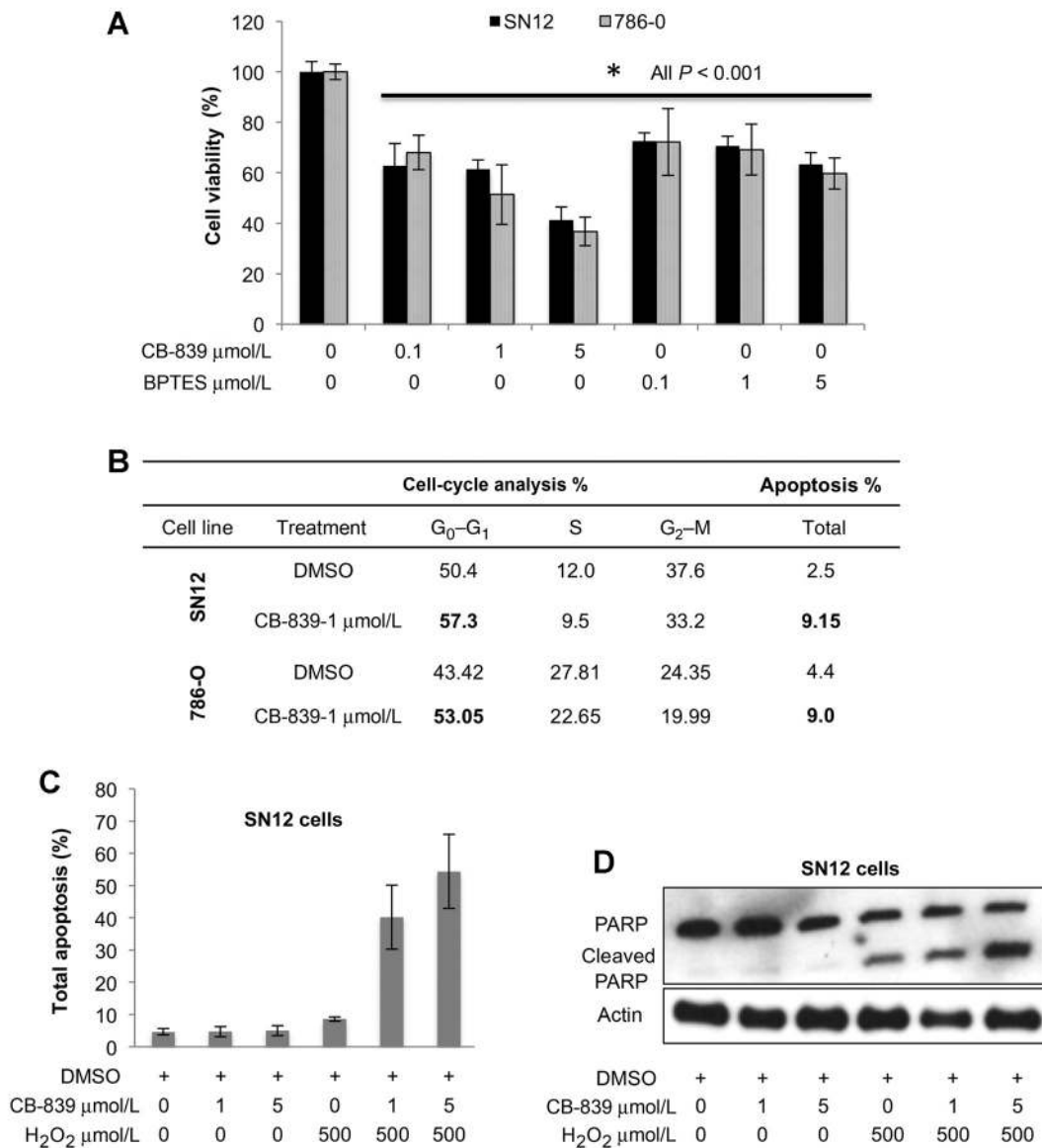
Figure 3.
CB-839 inhibits RCC cell viability by inducing both cell-cycle arrest and apoptosis in SN12 and 786-O RCC cells. **A,** SN12 and 786-O cells were grown and incubated with DMSO, CB-839, or BPTES at the concentrations indicated for 72 hours ($n = 8$ wells/group) and then subjected to MTT assay. Data are mean $\pm$ SD. *, $P < 0.001$ compared with DMSO control. Results shown are representative of at least three independent experiments. **B,** SN12 and 786-O cells were grown and incubated with CB-839 or DMSO (1 μmol/L) for 72 hours ($n = 3$/group). Cell-cycle populations and total apoptosis were measured by flow cytometry of stained cells. Results shown are representative of at least three independent experiments. **C,** SN12 cells were grown and incubated with CB-839 at the concentrations indicated for 20 hours, followed by 4-hour H_2O_2 where indicated ($n = 3$/group). Total apoptosis was measured by Annexin V and 7-AAD staining using flow cytometry. Percentages of total apoptosis are plotted. The results shown are representative of at least three independent experiments. Data are mean $\pm$ SD. **D,** At the same conditions in **C**, levels of cleaved PARP were measured by immunoblotting. The results shown are representative of at least three independent experiments.

In light of the fact that FDG-PET is challenging for RCC diagnosis and staging (31, 32), we next asked, based on our findings here and in previous publications of glutamine requirements of RCC (19), whether ^{18}F-FGln-PET could be employed for *in vivo* monitoring of this cancer. After confirming that SN12 as well as 786-O cells uptake 4-[^{18}F]fluoroglutamine *in vitro* (Fig. 6A) and that CB-839

resulted in tracer retention in SN12 cells (Fig. 6B), we subjected the mice to ^{18}F-FGln-PET and CT scanning immediately prior to starting treatments (day 0; Supplementary Fig. S5; Fig. 6C) and after 2 weeks of CB-839 treatment (day 14; Supplementary Fig. S5; Fig. 6C). The PET images were acquired 4 hours after the last dose of CB-839, which has been shown to be sufficient time for CB-839
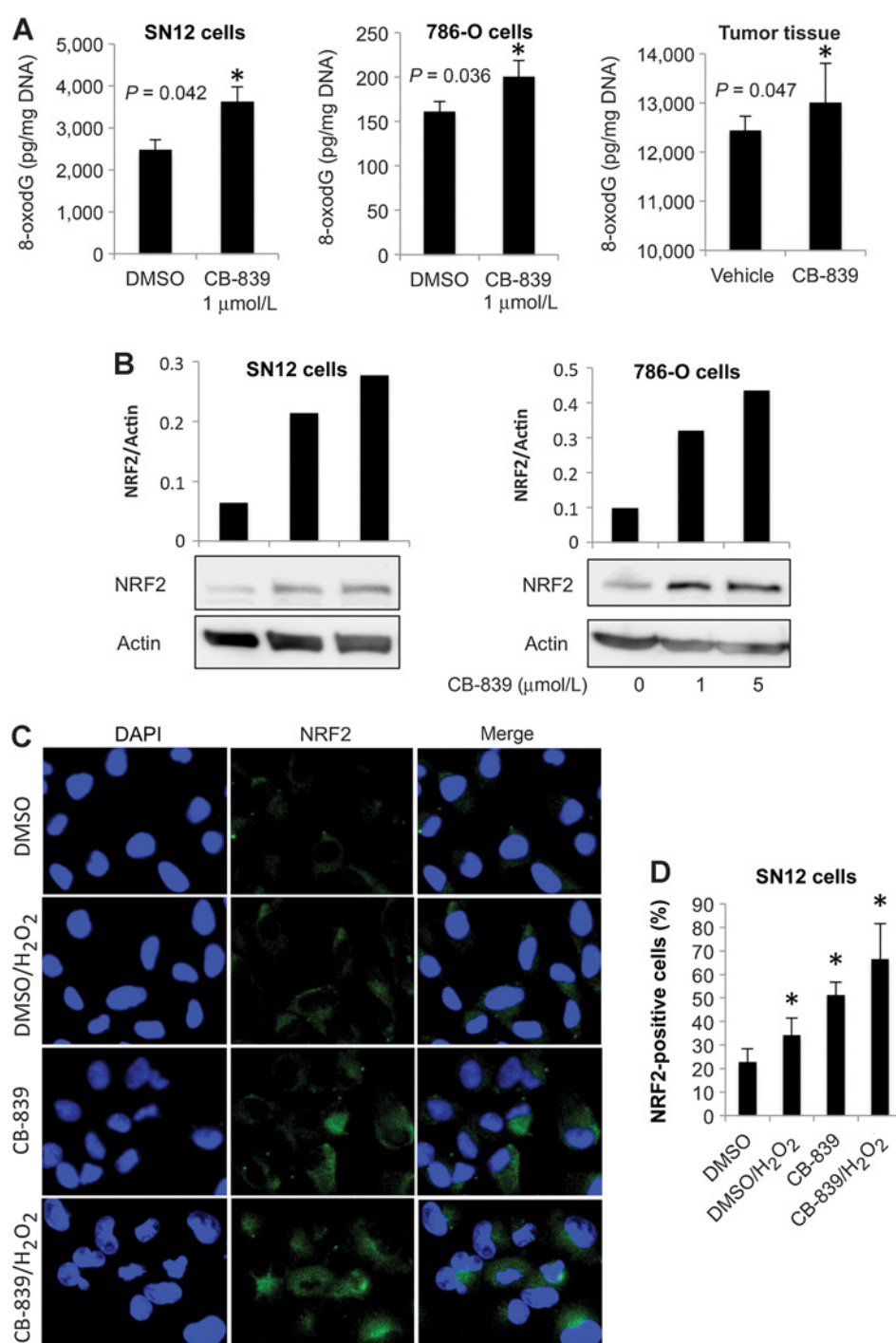
Figure 4.
Glutaminase inhibition augments oxidative stress in SN12 and 786-O cells and tumor tissue. **A,** SN12 and 786-O cells were grown, incubated with 1 μmol/L CB-839 or DMSO for 24 hours, and 8-oxodG levels were measured (left plots). Data are mean ± SD. *, $P < 0.05$ compared with control (DMSO). Tumor tissues from the second animal experiment (orally dosed with vehicle or CB-839) were harvested, and 8-oxodG levels were quantified (right plot). Data are mean ± SEM. *, $P < 0.05$ vehicle-treated group as compared with CB-839–treated group ($n = 4$). **B,** SN12 and 786-O cells were grown and incubated with CB-839 or DMSO at the concentrations indicated for 24 hours. NRF2 levels in whole-cell lysates were measured by immunoblotting. Densitometry relative to loading controls is shown. **C,** SN12 cells were grown and treated with CB-839 or DMSO at the concentrations and time indicated, followed by H_2O_2 treatment (where indicated) for 4 hours. The cells were fixed and subjected to immunofluorescence staining with NRF2 (green) and DAPI (blue), and then visualized with confocal laser-scanning microscopy. The results shown are representative of at least two independent experiments. **D,** For each treatment in **C,** five randomly selected microscopic fields (×40) of NRF2 positively stained cells were counted. Data are mean ± SD. *, $P < 0.05$ compared with DMSO control.
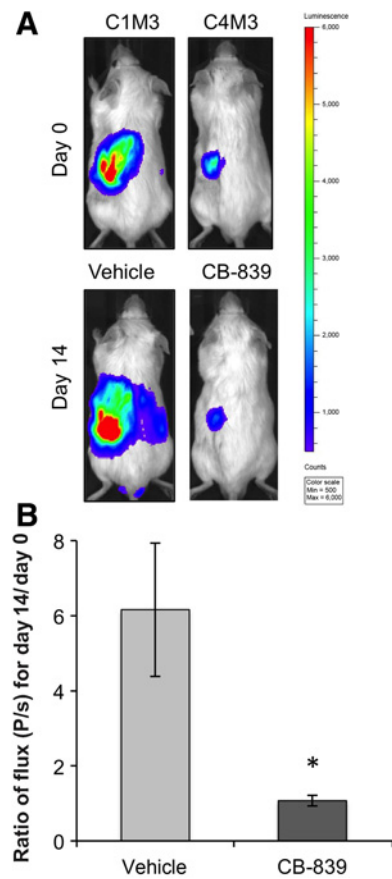
Figure 5.
CB-839 significantly attenuates tumor growth in an orthotopic RCC mouse model. **A,** SN12 cells were injected under the LK capsule of SCID mice ($n = 8$ per condition; third animal experiment). After 3 weeks, two mice were dosed orally twice a day with vehicle or 200 mg/kg CB-839 for 2 weeks. Weekly BLIs were performed to monitor tumor progression. _In vivo_ BLI for one representative mouse per group before and after CB-839 treatment is shown demonstrating significant reduction in tumor growth with CB-839 after 2 weeks. Color scale for all images was set on a minimum of 500 and a maximum of 6,000 counts. **B,** ROIs for all BLI images ($n = 8$ mice per group) before and after treatment were designated inside the primary tumor sites on the LK and quantified as a mean of total flux [photons/second (P/s)] using the Living Image software. The ratio of flux (P/s) at day 14/day 0 for each animal was calculated, and the average presented for each treatment group. Data are mean ± SEM. *, $P = 0.013$.

to be internalized in tumors and other tissues (29). The subcapsular xenografted tumors were visualized by ^{18}F-FGln uptake, as demonstrated by significantly higher uptake compared with the contralateral kidney (Fig. 6C and D). On day 0, the tumor SUV was 4.8, and the kidneys were 2.5. On day 14 in the vehicle-treated animals, the tumor SUV was 5.2, and the kidneys were 3.1. In addition, the kidneys and tumors both increased their 4-[^{18}F]fluoroglutamine uptake after treatment with CB-839 ($P = 0.026$; Fig. 6D), as expected from the _in vitro_ data (see Fig. 6B) as well as a recently published study in breast cancer (37).

Discussion

In aerobic conditions, rapidly proliferating cancer cells are invariably exposed to metabolites that produce oxidative stress
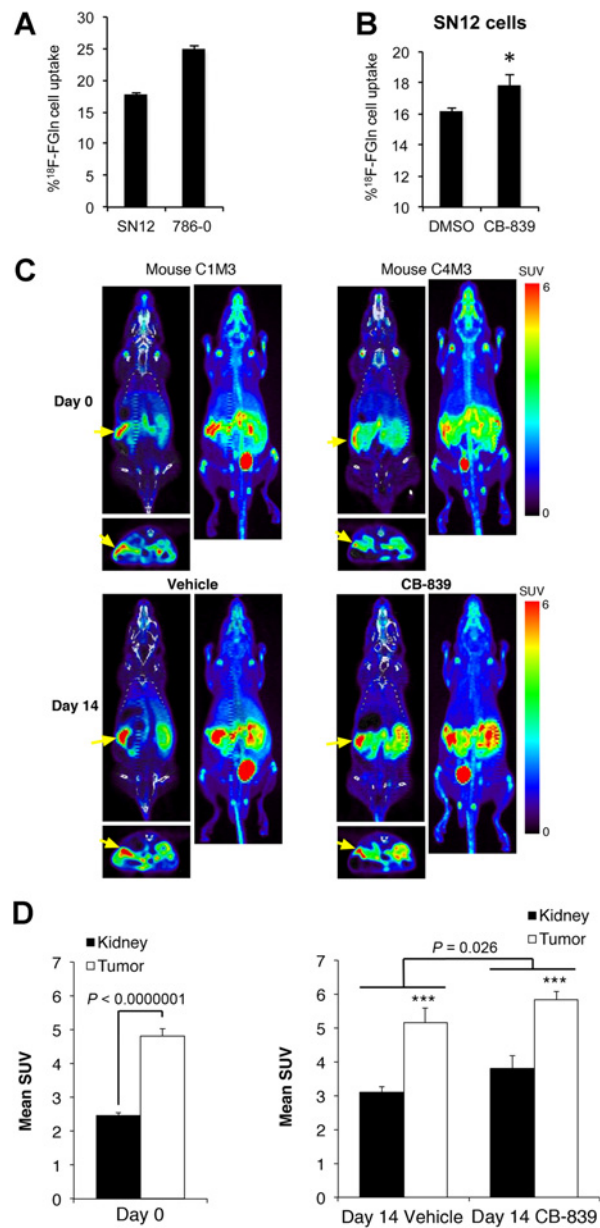

Figure 6.
^{18}F-FGln cell uptake and 4-[^{18}F]fluoroglutamine-PET imaging. **A,** Intracellular uptake of a 4-[^{18}F]fluoroglutamine tracer after 30-minute incubation in SN12 and 786-O RCC cell lines ($n = 3$ for each cell line). The y-axis represents percent uptake of total radioactivity by the cells. Data are mean ± SD. **B,** 4-[^{18}F]fluoroglutamine uptake in SN12 cells after 4-hour incubation with 1 μmol/L CB-839 ($n = 3$) or DMSO ($n = 3$) and 30 minutes with the 4-[^{18}F]fluoroglutamine. The y-axis represents percentage of total radioactivity contained in each group of cells. Data are mean ± SD. *, $P < 0.05$ compared with DMSO control. **C,** Representative mouse images from each treatment group are presented. Coronal and axial sections from PET (color) are overlaid on CT images (grayscale). Adjacent to each coronal PET/CT image is the coronal whole-body maximum intensity projection generated from the PET. Yellow arrows, tumors. **D,** Comparison of ^{18}F-FGln uptake in the tumors compared with the normal RKs at day 0 ($n = 10$) and day 14 of treatment ($n = 5$/group). Two ROIs (19.06 mm^3 ellipsoids) were drawn on the PET images of each mouse, one on the tumor and one on the RK. Mean SUV of ^{18}F-FGln for each ROI was calculated using AMIDE software. Data are mean ± SEM. ***, $P = 0.002$ for tumor compared with RK.

(49); thus, "successful" malignancies and metastases are those that are able to withstand such conditions through the production of intrinsic antioxidants (7, 8). Indeed, there are several recent reports that demonstrate that, contrary to lay press reports of antioxidants being beneficial dietary supplements (7), these compounds can in fact accelerate lung cancer progression in mice (13) and promote distant metastases in human melanoma cells (50, 51); similar findings have most recently been shown in pancreatic cancer by deletion of malic enzyme 2 (52). Although ccRCC cells have been shown to require glutamine for growth and survival (19), the direct role of this amino acid in the response of ccRCC cells and kidney cancers to oxidative stress has, prior to the current study, not been described.

Although our previous study suggested that the conditionally essential amino acid glutamine is required for production of the oxidative stress "buffers" GSH and GSSG (19), we now show that decreasing intracellular glutamate by the GLS inhibitor CB-839 (by blocking glutamine conversion to glutamate) has the direct effect of decreasing production of these buffers *in vitro* and *in vivo*. This in turn leads to an increase in oxidative stress with its resulting increase in DNA damage, which likely serves to attenuate growth of these tumors *in vivo*. These data are supported by a melanoma model of lymph node metastases, where an opposite approach to ours was used; in that study, administration of exogenous antioxidants resulted in increased levels of GSH synthesis (increase in ratio of GSH/GSSG) that was associated with increased metastases (51).

Because cancer cells possess many of the qualities of normal cells, they too can be damaged by ROS. Indeed, for a variety of reasons (53), cancer cells actually generate more ROS than normal cells and hence show more evidence of DNA damage and buffer system engagement (as we showed in this study), requiring them to have a greater antioxidant capacity. Such intrinsic antioxidants are thus required of "successful" cancers to reduce distant ROS damage while simultaneously allowing localized ROS signaling that promotes cell proliferation and survival (8). It is conceivable (7, 8) that systemic antioxidants, taken by many individuals in the hope that they are generally beneficial, could ultimately adversely affect ccRCC; thus, our data presented here could affect public health with respect to a cancer type that is growing in incidence and is lacking effective therapies.

Although there exists a robust and profitable industry that sells antioxidant supplements for a variety of ailments including cancer, there are few positive studies of such supplements in prolonging lifespan of cancer patients (8). That protection from oxidative stress plays a role in cancer progression and metastasis is only recently becoming apparent, and we and others have shown data suggestive that metabolic reprogramming of the glutamine and NADH pathways is responsible for this state of affairs, at least in kidney cancer (19, 23). Based on our work in this study elucidating the mechanism of their action, additional drugs targeting glutamine reprogramming are ripe for clinical trials; indeed a phase I trial of the glutaminase inhibitor CB-839 was the first salvo in applying this paradigm to RCC (although in that study CB-839 was compared with a combination therapy; ref. 30). In addition, dissuading patients with RCC from taking over-the-counter antioxidants may now be appropriate.

Although ^{18}F-FDG-PET is frequently used both to screen for and stage cancers, it has (despite highly reprogrammed aerobic glycolysis; refs. 19, 54) been problematic for ccRCC and is therefore not commonly used in the clinic for routine RCC staging (31, 32). Furthermore, the use of ^{18}F-FGln-PET has recently been developed for glioma (36, 55) and other tumors (35, 37). Capitalizing on glutamine reprogramming in antioxidant production in RCC and the inhibition of ccRCC tumor growth by the GLS inhibitor CB-839 as described in this study, we evaluated ^{18}F-FGln-PET in our *in vivo* RCC model and found that it successfully detected ccRCC tumors in our orthotopic mouse model. As proof of the likelihood of using this technique to monitor therapeutic response, we further showed, despite a decrease in tumor growth as evaluated by BLI, an increase in ^{18}F-FGln uptake in response to glutaminase inhibition with CB-839; the latter is consistent both with our cell culture uptake studies for ^{18}F-FGln reported here and a very recent study in breast cancer (37). Our study thus demonstrates that such glutamine dependence can potentially be evaluated using ^{18}F-FGln-PET imaging and could lead to stratification of patients into those whose tumors are more glutamine avid and are thus more likely to respond to glutaminase inhibition. We also show here that this approach could be amenable to *in vivo* monitoring of the progress of these tumors to glutaminase inhibition therapy by following the effect on tumoral glutamine in the presence of CB-839 or other glutaminase inhibitors. This is the first time to our knowledge that this technique has been used in identifying and imaging kidney malignancy under basal as well as therapeutic conditions.

The limitations of our study relate principally to the mouse model and cell line used, because, given the known heterogeneity of RCC (56), it is likely that human tumors will have variable degrees of oxidative stress depending on the makeup of their tumors. Consistent with this, and dependent on the degree of angiogenesis within each tumor, it is possible that CB-839 will have variable penetration into the tumor and hence inconsistent effect on both oxidative stress and tumor growth.

In summary, we have shown in this study that a glutamine-dependent antioxidant effect is present in ccRCC and likely provides this malignancy with a key mechanism for its survival in a hostile host environment. Furthermore, this reprogrammed pathway not only suggests an Achilles' heel that can be exploited by glutaminase inhibitors but also provides a means to use ^{18}F-FGln-PET imaging for diagnosis, stratification, and real-time response to therapy. Continuing translation of CB-839 and other inhibitors of the reprogrammed glutamine pathway to human trials, either singly or in combination with other therapies, has the potential to revolutionize clinical management of a cancer that is increasing in incidence and that currently has woefully limited treatment options.

Disclosure of Potential Conflicts of Interest

No potential conflicts of interest were disclosed.

Authors' Contributions

Conception and design: O.A. Aboud, S.L. Habib, J. Sutcliffe, R.H. Weiss
Development of methodology: O.A. Aboud, S.L. Habib, A.J. Chaudhari
Acquisition of data (provided animals, acquired and managed patients, provided facilities, etc.): O.A. Aboud, J. Trott, B. Stewart, S. Liang, A.J. Chaudhari, J. Sutcliffe
Analysis and interpretation of data (e.g., statistical analysis, biostatistics, computational analysis): O.A. Aboud, J. Trott, A.J. Chaudhari, J. Sutcliffe, R.H. Weiss

Acknowledgments

References

1. Day AM, Brown JD, Taylor SR, Rand JD, Morgan BA, Veal EA. Inactivation of a peroxiredoxin by hydrogen peroxide is critical for thioredoxin-mediated repair of oxidized proteins and cell survival. Mol Cell 2012;45:398–408.
2. Schieber M, Chandel NS. ROS function in redox signaling and oxidative stress. Curr Biol 2014;24:R453–62.
3. Wu Q, Ni X. ROS-mediated DNA methylation pattern alterations in carcinogenesis. Curr Drug Targets 2015;16:13–9.
4. Bielski BH, Arudi RL, Sutherland MW. A study of the reactivity of HO2/O2- with unsaturated fatty acids. J Biol Chem 1983;258:4759–61.
5. Finkel T. Redox-dependent signal transduction. FEBS Lett 2000;476:52–4.
6. Jabs T. Reactive oxygen intermediates as mediators of programmed cell death in plants and animals. Biochem Pharmacol 1999;57:231–45.
7. Herraiz C, Crosas-Molist E, Sanz-Moreno V. Reactive oxygen species and tumor dissemination: allies no longer. Mol Cell Oncol 2016;3:e1127313.
8. Chandel NS, Tuveson DA. The promise and perils of antioxidants for cancer patients. N Engl J Med 2014;371:177–8.
9. Gorrini C, Harris IS, Mak TW. Modulation of oxidative stress as an anticancer strategy. Nat Rev Drug Discov 2013;12:931–47.
10. Sabharwal SS, Schumacker PT. Mitochondrial ROS in cancer: initiators, amplifiers or an Achilles' heel? Nat Rev Cancer 2014;14:709–21.
11. Gao P, Zhang H, Dinavahi R, Li F, Xiang Y, Raman V, et al. HIF-dependent antitumorigenic effect of antioxidants in vivo. Cancer Cell 2007;12:230–8.
12. Patterson RE, White E, Kristal AR, Neuhouser ML, Potter JD. Vitamin supplements and cancer risk: the epidemiologic evidence. Cancer Causes Control 1997;8:786–802.
13. Sayin VI, Ibrahim MX, Larsson E, Nilsson JA, Lindahl P, Bergo MO. Antioxidants accelerate lung cancer progression in mice. Sci Transl Med 2014;6:221ra15.
14. Wang H, Liu X, Long M, Huang Y, Zhang L, Zhang R, et al. NRF2 activa-tion by antioxidant antidiabetic agents accelerates tumor metastasis. Sci Trans Med 2016;8:334ra51.
15. Cantor JR, Sabatini DM. Cancer cell metabolism: one hallmark, many faces. Cancer Discov 2012;2:881–98.
16. Hanahan D, Weinberg RA. Hallmarks of cancer: the next generation. Cell 2011;144:646–74.
17. Chen L, Cui H. Targeting glutamine induces apoptosis: a cancer therapy approach. Int J Mol Sci 2015;16:22830–55.
18. Hensley CT, Wasti AT, DeBerardinis RJ. Glutamine and cancer: cell biology, physiology, and clinical opportunities. J Clin Invest 2013;123:3678–84.
19. Wettersten HI, Hakimi AA, Morin D, Bianchi C, Johnstone ME, Donohoe DR, et al. Grade-dependent metabolic reprogramming in kidney cancer revealed by combined proteomics and metabolomics analysis. Cancer Res 2015;75:2541–52.
20. Wettersten HI, Aboud OA, Lara PN Jr., Weiss RH. Metabolic reprogram-ming in clear cell renal cell carcinoma. Nat Rev Nephrol 2017;13:410–9.
21. Ballatori N, Krance SM, Notenboom S, Shi S, Tieu K, Hammond CL. Glutathione dysregulation and the etiology and progression of human diseases. Biol Chem 2009;390:191–214.
22. Shim EH, Livi CB, Rakheja D, Tan J, Benson D, Parekh V, et al. L-2-Hydroxyglutarate: an epigenetic modifier and putative oncometabolite in renal cancer. Cancer Discov 2014;4:1290–8.
23. Wise DR, Thompson CB. Glutamine addiction: a new therapeutic target in cancer. Trends Biochem Sci 2010;35:427–33.
24. Hakimi AA, Reznik E, Lee CH, Creighton CJ, Brannon AR, Luna A, et al. An integrated metabolic atlas of clear cell renal cell carcinoma. Cancer Cell 2016;29:104–16.
25. Katt WP, Lukey MJ, Cerione RA. A tale of two glutaminases: homologous enzymes with distinct roles in tumorigenesis. Fut Med Chem 2017;9:223–43.
26. Lee YZ, Yang CW, Chang HY, Hsu HY, Chen IS, Chang HS, et al. Discovery of selective inhibitors of Glutaminase-2, which inhibit mTORC1, activate autophagy and inhibit proliferation in cancer cells. Oncotarget 2014;5:6087–101.
27. Gao P, Tchernyshyov I, Chang TC, Lee YS, Kita K, Ochi T, et al. c-Myc suppression of miR-23a/b enhances mitochondrial glutaminase expres-sion and glutamine metabolism. Nature 2009;458:762–5.
28. Wang JB, Erickson JW, Fuji R, Ramachandran S, Gao P, Dinavahi R, et al. Targeting mitochondrial glutaminase activity inhibits oncogenic transfor-mation. Cancer Cell 2010;18:207–19.
29. Gross MI, Demo SD, Dennison JB, Chen L, Chernov-Rogan T, Goyal B, et al. Antitumor activity of the glutaminase inhibitor CB-839 in triple-negative breast cancer. Mol Cancer Ther 2014;13:890–901.
30. Meric-Bernstam F, Tannir NMH, J J, Bennett MK. Phase 1 study of CB-839, a small molecule inhibitor of glutaminase (GLS), alone and in combination with everolimus (E) in patients (pts) with renal cell cancer (RCC). J Clin Oncol 2016;34.
31. Aide N, Cappele O, Bottet P, Bensadoun H, Regeasse A, Comoz F, et al. Efficiency of [(18)F]FDG PET in characterising renal cancer and detecting distant metastases: a comparison with CT. Eur J Nucl Med Mol Imaging 2003;30:1236–45.
32. Gofrit ON, Orevi M. Diagnostic challenges in kidney cancer: a systematic review of the role of PET/CT. J Urol 2016;196:648–57.
33. Shroff EH, Eberlin LS, Dang VM, Gouw AM, Gabay M, Adam SJ, et al. MYC oncogene overexpression drives renal cell carcinoma in a mouse model through glutamine metabolism. Proc Natl Acad Sci USA 2015;112:6539–44.
34. Gameiro PA, Yang J, Metelo AM, Perez-Carro R, Baker R, Wang Z, et al. In vivo HIF-mediated reductive carboxylation is regulated by citrate levels and sensitizes VHL-deficient cells to glutamine deprivation. Cell Metab 2013;17:372–85.
35. Lieberman BP, Ploessl K, Wang L, Qu W, Zha Z, Wise DR, et al. PET imaging of glutaminolysis in tumors by 18F-(2S,4R)4-fluoroglutamine. J Nucl Med 2011;52:1947–55.
36. Venneti S, Dunphy MP, Zhang H, Pitter KL, Zanzonico P, Campos C, et al. Glutamine-based PET imaging facilitates enhanced metabolic evaluation of gliomas in vivo. Sci Transl Med 2015;7:274ra17.

37. Zhou R, Pantel AR, Li S, Lieberman BP, Ploessl K, Choi H, et al. [18F]
(2S,4R)4-fluoroglutamine PET detects glutamine pool size changes in
triple negative breast cancer in response to glutaminase inhibition. Cancer
Res 2017;77:1476–84.

38. Jedeszko C, Paez-Ribes M, Di DT, Man S, Lee CR, Xu P, et al. Postsurgical
adjuvant or metastatic renal cell carcinoma therapy models reveal potent
antitumor activity of metronomic oral topotecan with pazopanib. Sci
Transl Med 2015;7:282ra50.

39. Guo S, Duan JA, Qian D, Tang Y, Qian Y, Wu D, et al. Rapid determi-
nation of amino acids in fruits of Ziziphus jujuba by hydrophilic
interaction ultra-high-performance liquid chromatography coupled
with triple-quadrupole mass spectrometry. J Agr Food Chem 2013;
61:2709–19.

40. Ganti S, Taylor SL, Abu AO, Yang J, Evans C, Osier MV, et al. Kidney tumor
biomarkers revealed by simultaneous multiple matrix metabolomics anal-
ysis. Cancer Res 2012;72:3471–9.

41. Abu Aboud O, Chen CH, Senapedis W, Baloglu E, Argueta C, Weiss RH.
Dual and specific inhibition of NAMPT and PAK4 by KPT-9274 decreases
kidney cancer growth. Mol Cancer Ther 2016;15:2119–29.

42. Habib SL, Phan MN, Patel SK, Li D, Monks TJ, Lau SS. Reduced constitutive
8-oxoguanine-DNA glycosylase expression and impaired induction fol-
lowing oxidative DNA damage in the tuberin deficient Eker rat. Carcino-
genesis 2003;24:573–82.

43. Qu W, Zha Z, Ploessl K, Lieberman BP, Zhu L, Wise DR, et al. Synthesis of
optically pure 4-fluoro-glutamines as potential metabolic imaging agents
for tumors. J Am Chem Soc 2011;133:1122–33.

44. Jones DP.Redox potential of GSH/GSSG couple: assay and biological
significance. Methods Enzymol 2002;348:93–112.

45. Zitka O, Skalickova S, Gumulec J, Masarik M, Adam V, Hubalek J, et al.
Redox status expressed as GSH:GSSG ratio as a marker for oxidative stress in
paediatric tumour patients. Oncol Lett 2012;4:1247–53.

46. Li W, Kong AN. Molecular mechanisms of Nrf2-mediated antioxidant
response. Mol Carcinog 2009;48:91–104.

47. Shibutani S, Takeshita M, Grollman AP. Insertion of specific bases during
DNA synthesis past the oxidation-damaged base 8-oxodG. Nature 1991;
349:431–4.

48. Hwang VJ, Kim J, Rand A, Yang C, Sturdivant S, Hammock B, et al. The cpk
model of recessive PKD shows glutamine dependence associated with the
production of the oncometabolite 2-hydroxyglutarate. Am J Physiol Renal
Physiol 2015;309:F492–F8.

49. Gupta SC, Hevia D, Patchva S, Park B, Koh W, Aggarwal BB. Upsides and
downsides of reactive oxygen species for cancer: the roles of reactive oxygen
species in tumorigenesis, prevention, and therapy. Antioxidants Redox
Signal 2012;16:1295–322.

50. Piskounova E, Agathocleous M, Murphy MM, Hu Z, Huddlestun SE, Zhao
Z, et al. Oxidative stress inhibits distant metastasis by human melanoma
cells. Nature 2015;527:186–91.

51. Le GK, Ibrahim MX, Wiel C, Sayin VI, Akula MK, Karlsson C, et al.
Antioxidants can increase melanoma metastasis in mice. Sci Transl Med
2015;7:308re8.

52. Dey P, Baddour J, Muller F, Wu CC, Wang H, Liao WT, et al. Genomic
deletion of malic enzyme 2 confers collateral lethality in pancreatic cancer.
Nature 2017;542:119–23.

53. Morry J, Ngamcherdtrakul W, Yantasee W. Oxidative stress in cancer
and fibrosis: opportunity for therapeutic intervention with antioxidant
compounds, enzymes, and nanoparticles. Redox Biol 2016;11:
240–53.

54. Perroud B, Ishimaru T, Borowsky AD, Weiss RH. Grade-dependent prote-
omics characterization of kidney cancer. Mol Cell Proteomics 2008;8:
971–85.

55. Qu W, Oya S, Lieberman BP, Ploessl K, Wang L, Wise DR, et al. Preparation
and characterization of L-[5–11C]-glutamine for metabolic imaging of
tumors. J Nucl Med 2012;53:98–105.

56. Gerlinger M, Rowan AJ, Horswell S, Larkin J, Endesfelder D, Gronroos E,
et al. Intratumor heterogeneity and branched evolution revealed by multi-
region sequencing. N Engl J Med 2012;366:883–92.